PHYSICAL REVIEW LETTERS **128,** 068102 (2022)

Dynamics and Stability of the Contractile Actomyosin Ring in the Cell

Mainak Chatterjee,[*] Arkya Chatterjee,[*,†] Amitabha Nandi, and Anirban Sain[‡]
Department of Physics, Indian Institute of Technology-Bombay, Powai, Mumbai 400076, India

(Received 29 May 2020; revised 13 December 2021; accepted 18 January 2022; published 11 February 2022)

Contraction of the cytokinetic ring during cell division leads to physical partitioning of a eukaryotic cell into two daughter cells. This involves flows of actin filaments and myosin motors in the growing membrane interface at the midplane of the dividing cell. Assuming boundary driven alignment of the actomyosin filaments at the inner edge of the interface, we explore how the resulting active stresses influence the flow. Using the continuum gel theory framework, we obtain exact axisymmetric solutions of the dynamical equations. These solutions are consistent with experimental observations on closure rate. Using these solutions, we perform linear stability analysis for the contracting ring under nonaxisymmetric deformations. Our analysis shows that few low wave number modes, which are unstable during onset of the constriction, later on become stable when the ring shrinks to smaller radii, which is a generic feature of actomyosin ring closure. Our theory also captures how the effective tension in the ring decreases with its radius, causing significant slowdown in the contraction process at later times.

DOI: 10.1103/PhysRevLett.128.068102

Cell division is fundamental to all living organisms. The last stage of cell division is called cytokinesis, where closure of a polymeric ring, made of actin filaments and myosin molecular motors [1,2] completes the physical partitioning of the cell. In one mode of partitioning, an intercellular membrane forms [see Fig. 1(a)]. This is common in mitotic cell divisions (e.g., in *C. elegans* embryo, a widely studied model system for eukaryotes) and also in some compact tissues [3]. In the other mode [see Fig. 1(b)], the contact area between the daughter cells gradually shrinks to zero, as the division furrow [the cusp in Fig. 1(b)] caves in [4]. Here we focus on the development of the intercellular membrane (the first mode), which starts out as an annulus at the equatorial plane [see Figs. 1(a) and 1(c)] and gradually closes itself, as its inner boundary grows radially inward. The growth is assisted by the flow of actomyosin, beneath the cell surface (the "cortical flow") [5]. Experiments suggest [1,2,6] that the adenosine triphosphate (ATP) driven interaction between actin and myosin leads to the generation of *active* contractile stresses in the cytokinetic ring. How this stress changes with time during the course of the constriction, however, is not clear. Earlier models [4,7] explain the observed contraction rate by assuming a constant contractile stress. Sain *et al.* [8] had, in addition, assumed an *ad hoc* intrinsic dynamic friction, to account for the eventual slowdown of the contraction process.

Such an approach, which considers the actin ring to be a separate entity attached with the growing active membrane, cannot explain the recent experimental observations [9] where the ring is found to reorganize and constrict even after part of it is destroyed by localized laser ablation. This motivates us to consider the cortical ring to be part of the actomyosin continuum spread over the growing membrane interface. In Ref. [10], the authors developed an active gel model of the cytoskeletal flows to discuss wound healing in *Xenopus* oocyte [11]. Such a description involves solution of coupled equations for the actin alignment field $Q_{\alpha\beta}(r)$ (the order parameter, OP) and the velocity field $v_\alpha(r)$. The ring was assumed to be a narrow annular zone with a higher

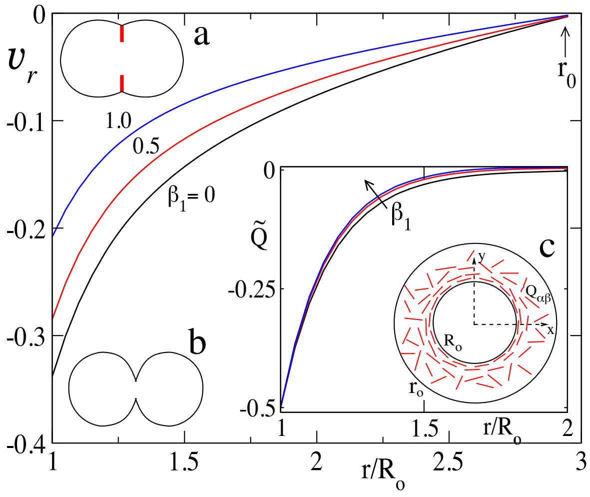

FIG. 1. Radial velocity field $v_r(r)$ (main figure), in units of $L_c/(\tilde{\eta}/\zeta\Delta\mu)$ and OP field $\tilde{Q}(r)$ (inset) are shown as a function of r/R_0, for $R_0 = 5\ \mu$m. Schematic diagram (a) shows a side view of the growing interface at the middle of the cell and (c) shows its cross-sectional view; (b) shows partitioning without an interface. In diagram (c) alignment of filaments increases sharply near the inner boundary of the annulus at R_0. The outer boundary is fixed at $r_0 = 15\ \mu$m for both the plots in the main and the inset.

0031-9007/22/128(6)/068102(5)

level of myosin activity $\zeta\Delta\mu$ than the rest of the growing interface.

In this Letter, we follow a similar continuum gel theory approach and first solve the coupled equations for the OP and the velocity fields numerically (Fig. 1), retaining flow coupling. However, instead of assuming an active contractility gradient, which is standard in the literature [10], we use the observation that actin filaments are aligned tangentially to the inner boundary of the closing annulus [12,13] as a boundary condition. This is motivated by recent experiments [14,15] which indicate that local assembly kinetics, like guided polymerization, can drive rapid filament alignment at the ring at a much faster rate compared to the relatively slow hydrodynamic modes of the OP and the flow fields. The mean (time-averaged) effect of this molecular level, fast, alignment kinetics can be incorporated in the hydrodynamic equation for the OP field as a boundary condition. Such a boundary driven alignment was used in Refs. [16,17] to solve for the OP field. Chen *et al.* [16] reported that actomyosin filaments at open cell boundaries can respond to the curvature of the boundary and align parallel or perpendicular to the concave or convex boundaries, respectively. Encouraged by these observations on boundary driven alignment, we set out to compute (a) the constriction rate of the cytokinetic ring and (b) its stability with respect to nonaxisymmetric deformations, which has wide applicability across eukaryotic cell division.

Active gel model for actomyosin filaments.—The actomyosin gel on the growing interface is modeled as a nematic fluid. Orientational order in a nematic fluid, in three dimensions, is defined by the tensor order parameter $Q_{\alpha\beta} = \langle n_\alpha n_\beta - \delta_{\alpha\beta}/3\rangle$, where n_α is the nematic director field, and $\alpha, \beta = (x, y, z)$. As the actomyosin filaments (nematic directors) lie in the flat interface (x–y), symmetry and tracelessness of $Q_{\alpha\beta}$ dictate that the nondiagonal matrix elements involving z are zero, $Q_{xy} = Q_{yx} = q$, $Q_{zz} = -1/3$, and $Q_{xx} + Q_{yy} = 1/3$. Further, if the orientation distribution is isotropic in the x–y plane, then the resulting matrix $Q^0_{\alpha\beta}$ is diagonal, with $Q^0_{xx} = Q^0_{yy} = 1/6$ and $Q^0_{zz} = -1/3$. In the presence of cortical flows or due to specific boundary conditions, the isotropic distribution is modified to $Q_{\alpha\beta} = Q^0_{\alpha\beta} + Q'_{\alpha\beta}$. Again symmetric structure and tracelessness of $Q_{\alpha\beta}$ require (see Supplemental Material [18]) that $Q'_{xx} = -Q'_{yy} = \tilde{Q}$, $Q'_{xy} = Q'_{yx} = q$, and the rest of the elements are zero. This form remains invariant as we transform from Cartesian to 2D polar coordinates later.

The free energy of the inhomogeneous nematic field can be described by the Landau–de Gennes form [19], using the Q' matrix. $\mathcal{F} = \int d^3r[(\chi/2)Q'_{ij}Q'_{ji} + (L/2)\partial_k Q'_{ij}\partial_k Q'_{ij}]$. This enforces an isotropic arrangement of the director field in the bulk of the 2D growing cortical layer with a correlation length $L_c = \sqrt{L/\chi}$. Later, we will see that this turns out to be the width of the actomyosin ring, which has been measured [20] to be ~ 1 μm.

Constitutive equations of the active gel can be described by a linear relationship between thermodynamic fluxes and forces [10,21–23]. We choose stress tensor $\sigma_{\alpha\beta}$, the rate of change of nematic order parameter $(DQ_{\alpha\beta}/Dt)$, and the rate of ATP consumption as the fluxes. The conjugate forces are the strain rate $v_{\alpha\beta} = \frac{1}{2}(\partial_\alpha v_\beta + \partial_\beta v_\alpha)$, the traceless nematic force field $H_{\alpha\beta} = -(\delta\mathcal{F}/\delta Q'_{\alpha\beta})$, and the chemical potential difference generated due to ATP hydrolysis $\Delta\mu$. Following [10], the hydrodynamic equations in the liquid limit can be expressed as follows:

$$\sigma_{\alpha\beta} = 2\eta v_{\alpha\beta} - \beta_1 H_{\alpha\beta} + \zeta\Delta\mu Q_{\alpha\beta}, \tag{1}$$

$$\frac{D}{Dt}Q_{\alpha\beta} = \beta_1 v_{\alpha\beta} + \frac{1}{\beta_2}H_{\alpha\beta}. \tag{2}$$

(D/Dt) here implies material derivative [21], $\zeta\Delta\mu Q_{\alpha\beta}$ is the active stress, and contractility of the cortical layer enforces $\zeta > 0$ [21,22]. We ignored any explicit active term in the second equation because it just renormalizes the inverse susceptibility χ^{-1}. Here η is the fluid viscosity, while β_1 and β_2 are Onsager coefficients [10] and give the flow coupling and nematic relaxation strengths, respectively [10].

Following [10], we define a 2D "tension tensor" t_{ij} via the relation $t_{ij} = \int(\sigma_{ij} - \delta_{ij}P)dz$. Imposing the net normal stress on the interface t_{zz} to be zero yields pressure $P = \sigma_{zz}$. Further, ignoring variation of stress across the thin interface, we get [10] $t_{ij} = e(\sigma_{ij} - \delta_{ij}\sigma_{zz})$, where e is the effective thickness of the interface, assumed to be a constant here. This tension tensor allows us to write a two-dimensional hydrodynamic theory with the force balance equation as $(\partial/\partial t)(\rho v_i) = \partial_j t_{ij} - \alpha v_i$. Here α is the cytoplasmic friction external to the growing membrane interface. The flat growing interface has an annular shape, see Fig. 1(c). The shrinking cytokinetic ring of radius $R_0(t)$ lies at its inner periphery, while its outer periphery is fixed at radius r_0. After changing to 2D polar coordinates and dropping the time derivative in the highly viscous regime, the force balance equations are $\partial_r t_{rr} + (1/r)(t_{rr} - t_{\theta\theta}) + (1/r)\partial_\theta t_{r\theta} = \alpha v_r$, and $\partial_r t_{\theta r} + (1/r)(t_{\theta r} + t_{r\theta}) + (1/r)\partial_\theta t_{\theta\theta} = \alpha v_\theta$ (see Supplemental Material [18]).

The $2 \times 2(xy)$ block of the $Q'_{\alpha\beta}$ matrix (anisotropic part) remains traceless and symmetric, parametrized by two variables $\tilde{Q}$ and q, although their values change in the polar frame. The 2×2 block of the isotropic matrix, however, remains unchanged, $Q^0_{\alpha\beta} = \mathbb{I}/6$, where $\mathbb{I}$ is the identity matrix (see Supplemental Material [18]).

Rotationally symmetric solutions for $Q'_{\alpha\beta}(r)$ and $v_\alpha(r)$.—We first consider the special case where the circular ring is at $r = R_0$, with our domain of interest $r \geq R_0$. We start with $\alpha = 0$, set a stress-free boundary condition at the open edge, i.e., normal stress $\sigma_{rr}(R_0) = 0$, and $v_r = 0$ at $r \to \infty$. The nematic directors are assumed to be parallel to the inner boundary, i.e., $\hat{n}(R_0) = \hat{\theta}$, and isotropic as $r \to \infty$. It implies that, at $r = R_0$, the anisotropic $Q'_{\alpha\beta}$ matrix is diagonal with $Q'_{rr} = -Q'_{\theta\theta} = \tilde{Q} = -1/2$ (see Supplemental Material [18]) and $Q'_{\alpha\beta}(r = \infty) = 0$.

We assume a quasisteady state where the material derivative $DQ_{\alpha\beta}/Dt = 0$ in Eq. (2). Note that $\partial Q_{\alpha\beta}/\partial t \neq 0$ since the inner edge R_0 keeps moving, but the convection term $\mathbf{v} \cdot \nabla Q_{\alpha\beta}$ counters this change to keep $Q_{\alpha\beta}$ unaltered in the material frame. This yields $H_{\alpha\beta} = -\beta_1\beta_2 v_{\alpha\beta}$. When expressed in polar form, the diagonal elements of this equation gives Eq. (3) below. However, the nondiagonal part yields $q = 0$ (see Supplemental Material [18]). Here we used $\beta_2 \approx \eta$ [10] and $\zeta\Delta\mu/\chi \simeq 1$,

$$\frac{1}{r}\partial_r(r\partial_r)\tilde{Q} - \left(\frac{1}{L_c^2} + \frac{4}{r^2}\right)\tilde{Q} = -\frac{\beta_1}{2L_c^2}\frac{\eta}{\zeta\Delta\mu}\left(\partial_r v_r - \frac{v_r}{r}\right). \tag{3}$$

Substitution of $H_{\alpha\beta} = -\beta_1\beta_2 v_{\alpha\beta}$ into Eq. (1) simply renormalizes the viscosity to $\tilde{\eta} = \eta[1 + (1/2)\beta_1^2]$. The resulting velocity equation (in polar form) using force balance yields

$$4\tilde{\eta}\partial_r\left(\partial_r + \frac{1}{r}\right)v_r = -\zeta\Delta\mu\left(\partial_r + \frac{2}{r}\right)\tilde{Q}. \tag{4}$$

Using zero influx $v_r(r_0) = 0$ at the outer boundary and a stress-free inner boundary $\sigma_{rr}(R_0) = 2\tilde{\eta}\partial_r v_r + (\zeta\Delta\mu/6) + \zeta\Delta\mu\tilde{Q} = 0$, we solve these two coupled equations numerically (using *Mathematica*) for different values of the flow coupling strength β_1. The solutions are shown in Fig. 1, using L_c as the unit of length and $(\tilde{\eta}/\zeta\Delta\mu)$ as the unit of time. It shows damping of the velocity field v_r with increase in flow coupling strength β_1. Therefore, stronger flow coupling delays the ring closure time; however, the order parameter profile, shown in the inset of Fig. 1, appears to be almost unaffected by flow coupling strength β_1. Note that, in this moving boundary problem, the major role of the flow coupling on the OP is to move the boundary inward where the actin field gets realigned quickly. By setting $\tilde{Q}(R_0) = -1/2$, we have already captured this effect indirectly. This important observation allows us to ignore flow coupling in the OP equation here [rhs of Eq. (3)], which can now be solved exactly. The general solution is $\tilde{Q}(r) = c_1 K_2(r/L_c) + c_2 I_2(r/L_c)$, where K_2 and I_2 are modified Bessel functions (see Supplemental Material [18]). For the outer boundary $r_0 \to \infty$, we get

$$\tilde{Q}(r) = -K_2(r/L_c)/2K_2(R_0/L_c). \tag{5}$$

The solution for finite r_0 is given in the Supplemental Material [18]. The sharp rise in the magnitude of $\tilde{Q}$ (irrespective of β_1) at the inner edge can be interpreted as the actomyosin ring, of width L_c. Using this solution, we can now solve for v_r [Eq. (4)] with arbitrary β_1. For $r_0 \to \infty$, the solution reads

$$\frac{v_r(r)}{\zeta\Delta\mu/\tilde{\eta}} = -\left[\left(1 + \frac{3K_1'(R_0/L_c)}{4K_2(R_0/L_c)}\right)\frac{R_0^2}{6r} + \frac{L_c}{8}\frac{K_1(r/L_c)}{K_2(R_0/L_c)}\right]. \tag{6}$$

Note that the velocity at $r = R_0$ is the ring closure rate $v_r(R_0) = -(\zeta\Delta\mu/\tilde{\eta})(R_0/6)[1 - \frac{3}{4}K_0(R_0/L_c)/K_2(R_0/L_c)]$, which is directly damped by the flow coupling strength β_1 via the effective viscosity $\tilde{\eta}$. Inclusion of cytoplasmic friction ($\alpha\mathbf{v}$), the velocity influx $v_r(r_0)$ at a finite outer boundary $r = r_0 > R_0$ (instead of $r_0 \to \infty$), can also influence the flow and the closure speed. Solutions for the boundary conditions $\tilde{Q}(r_0) = 0$ and $v_r(r_0) = 0$ are given in the Supplemental Material [18].

Cytoplasmic friction adds αv_r to the right-hand side of Eq. (4) but does not alter the equation for $\tilde{Q}$. Restricting ourselves to radial motion only (v_r nonzero, $v_\theta = 0$) and assuming azimuthal symmetry, we get

$$\left[\partial_r\left(\partial_r + \frac{1}{r}\right) - \frac{\alpha}{4\tilde{\eta}}\right]v_r = -\frac{\zeta\Delta\mu}{4\tilde{\eta}}\left(\partial_r + \frac{2}{r}\right)\tilde{Q}. \tag{7}$$

With boundary conditions $\tilde{Q}(r_0) = v_r(r_0) = 0$, and those at $r = R_0$ remaining the same as before, we solve Eq. (7), both using Green's function (see Supplemental Material [18]) and numerically in *Mathematica*. As expected, see Fig. 2, cytoplasmic friction damps the flow at the growing interface and slows down the ring closure speed (inset of Fig. 2).

The above analysis is carried out quasistatically for a fixed R_0. We can use these results to obtain the ring closure kinetics. We integrate the kinematic boundary condition $(d/dt)R_0 = v_r(R_0)$ to derive the time dependence of the radius of the contracting ring, i.e., R_0 versus t. In Fig. 2 (inset), we compare this closure rate with experimental data on *C. elegans* embryo [7,24]. Note that this is a three parameter fit with α, β_1, and the active timescale $(\tilde{\eta}/\zeta\Delta\mu)$. Reasonable fits can be obtained for several combinations of these parameters in the range $\alpha, \beta_1 \in [0.1, 0.5]$ and $(\tilde{\eta}/\zeta\Delta\mu) \in [1.5, 2.5]$ sec. One such example is shown in Fig. 2 (inset). Here we used $L_c = 1$ μm [24]. Membrane tension σ_0 in the growing membrane can be linked to the activity as $\sigma_0 = \zeta\Delta\mu e/2$ [10]. Using $(\tilde{\eta}/\zeta\Delta\mu) \simeq 2$ sec, measured value of cortical tension $\sigma_0 = 3 \times 10^{-4}$ N/m [25], and the thickness of the growing actomyosin cortex $e \simeq 0.3$ μm [24], we get $\tilde{\eta} \simeq 4 \times 10^3$Pa sec, which is similar to the estimates obtained in earlier works [10,26].

The ring closure rate in eukaryotes shows an intriguing slowdown at late times [Fig. 2 (inset)], which has not been

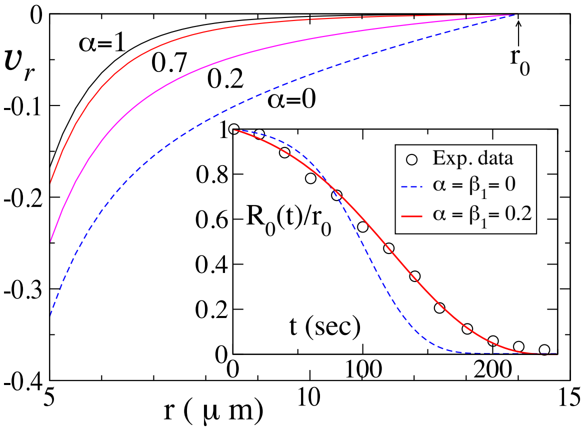

FIG. 2. Cytoplasmic friction slows down the flow: v_r versus r in the main plot for different friction coefficients α. Inset: lines show scaled radius of the ring $R_0(t)/r_0$ versus time (sec) for $\alpha, \beta_1 = 0$ and nonzero values (see legends), with $(\tilde{\eta}/\zeta\Delta\mu) = 2.06$ sec for both. Furthermore, $r_0 = 14$ μm and $v_r(r_0) = 0$. Circles are the experimental data on *C. elegans* embryo [7,24].

understood yet. In Ref. [8], an *ad hoc* intrinsic dynamic friction ζ_L was added to the ring tension to account for hitherto unknown internal processes in the ring. In Ref. [4], the cortical flow from the poles, converging toward the equatorial furrow [$v_r(r_0)$ in our theory], was shown to affect the slowdown [4]. In our present theory, $\sigma_{\theta\theta}(r = R_0)$ is the effective ring tension Σ of Ref. [8]. From Eq. (1),

$$\sigma_{\theta\theta} = 2\tilde{\eta}\frac{v_r}{r} + \frac{\zeta\Delta\mu}{6} - \zeta\Delta\mu\tilde{Q}. \tag{8}$$

In Fig. 3(a) we show the ring tension as a function of the ring size R_0, and Fig. 3(b) shows how azimuthal stress varies in the bulk of the closing interface, for a given ring size R_0. First, $\sigma_{\theta\theta}$ is always positive, implying contractile stress in the ring and the interface. Second, the ring tension falls sharply at small R_0, which explains the slowdown. Third, the azimuthal stress $\sigma_{\theta\theta}(r)$ is very high at the edge $r = R_0$ and small in the interior. This property perfectly justifies the role of the ring as the main generator of cytokinetic tension. Note, that in Eq. (8) the last two terms on the right-hand side are constants (at the ring $r = R_0$) and positive; however, the first term is negative and its magnitude grows large as the hole shrinks, eventually reducing the line tension. So the slowing down effect appears naturally due to viscosity of the flowing gel and curvature of the ring. Interestingly, this tension reduction term has the same structure $v_r(R_0)/R_0 = \dot{R}_0/R_0$ that was assumed in Ref. [8], based purely on phenomenology.

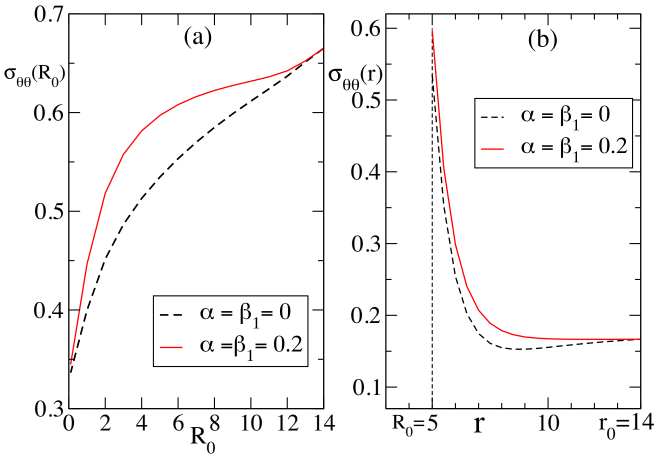

FIG. 3. The line tension [Eq. (8)] at the ring $\Sigma = \sigma_{\theta\theta}(R_0)$, in units of activity $\zeta\Delta\mu$, shown as a function of ring radius R_0 (a) and as a function of r (b), at a fixed $R_0 = 5$ μm. The outer radius is fixed at $r_0 = 14$ μm, appropriate for *C. elegans* embryo [7,24]. Friction (nonzero α) does not affect ring tension significantly.

Stability of ring closure.—We now use the rotationally symmetric solutions for the Q_{ij} and the **v** fields to examine the stability of the inner boundary where the ring forms. This is motivated by the observation that wild type rings, during constriction, typically show deviation from circular shape [9,24,27]; however, it becomes more circular as constriction proceeds. Toward this, we express the shape of the deformed inner boundary, at any given time, as $r(\theta) = R_0 + \delta R(\theta)$, and using Fourier decomposition $\delta R(\theta, t) = \sum_{n=0}^{\infty} \delta R_n e^{in\theta + \omega_n t}$. We study stability of these deformation modes [28] by computing ω_n, up to $n = 10$. Note that the $n = 1$ mode corresponds to a uniform translation of the inner circular boundary and, therefore, $\omega_1 = 0$. The system has translational symmetry provided the outer boundary $r_0 \to \infty$, which we use, along with $\beta_1 = \alpha = 0$, for this calculation. The results below are unlikely to change qualitatively when r_0 is finite, except that ω_1 will be nonzero.

The change at the inner edge leads to change in all the dynamical variables: $\tilde{Q}(r, \theta, t) = \tilde{Q}_0(r) + \delta\tilde{Q}(r, \theta, t)$, and similarly, $q(r, \theta, t) = \delta q(r, \theta, t)$, $v_r(r, \theta, t) = v_r^0(r) + \delta v_r(r, \theta, t)$, and $v_\theta(r, \theta, t) = \delta v_\theta(r, \theta, t)$. Here $\tilde{Q}_0$ and v_r^0 refer to solutions in Eqs. (5) and (6).

Further, the perturbation fields $\delta\tilde{Q}$, δq, δv_r, and δv_θ can be decomposed into Fourier modes as $\delta\tilde{Q}(r, \theta, t) = \sum_{n=0}^{\infty} \delta\tilde{Q}_n(r) e^{in\theta + \omega_n t}$, $\delta v_r(r, \theta, t) = \sum_{n=0}^{\infty} \delta v_{r,n}(r) e^{in\theta + \omega_n t}$, and similarly for the other two fields.

We substitute these perturbed fields in the dynamical equations and do a linear stability analysis to obtain $\{\omega_n\}$, where $\omega_n = \partial_r v_r^0(R_0) + [\delta v_{r,n}(R_0)/\delta R_n]$, following Ref. [28]. Details of our calculations are given in the Supplemental Material [18].

Figure 4 reveals interesting behavior for the growth rates of the Fourier modes $\{\omega_n\}$ for different inner radius R_0. At large R_0, several modes are unstable ($\omega_n > 0$), however, they subsequently turn stable ($\omega_n < 0$) as R_0 becomes small, absolutely consistent with experimental observations. Note that $\omega_0 < 0$, irrespective of R_0, implies stability with respect to uniform contraction or expansion of the circular inner boundary. While in our theory ω_n is exactly proportional to the activity, Fig. 4 shows that ω_0 is

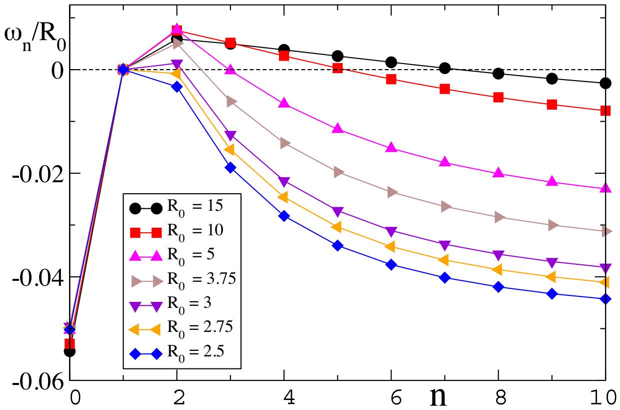

FIG. 4. ω_n, scaled by the inner radius R_0, as a function of the mode number n for different values of R_0 (micrometers), see legends. Low wave number modes switch from unstable to stable at smaller R_0.

approximately proportional to R_0. Also note that the higher modes decay relatively faster, which would make any sharp distortion of the ring heal fast. This could be relevant for wound healing in cells as well. However, the fact that a larger number of modes are unstable at larger ring size indicates that very large rings, if distorted, will fail to contract.

In summary, our phenomenological approximation on the boundary driven actomyosin alignment was useful in obtaining exact solutions for the OP and the velocity field. The stability calculation, which produced several insights, exploited these solutions to perturb around them. Also we could identify three separate sources of slowdown near the end of the constrictions, namely, (a) the curvature at the ring ($1/R_0$), (b) the cytoplasmic friction (α), and (c) the flow coupling strength (β_1). Experiments along the lines of Ref. [14], which probed poly- and depolymerization processes near the ring, and Ref. [9], which studied healing of the perturbed ring after laser ablation, might be useful to assess the role of boundary in maintaining actin alignment in the dynamic ring.

We thank one of the referees for pointing out Ref. [16] to us. M. C. would like to thank Industrial Research and Consultancy Centre (IRCC), IIT Bombay, India for financial support. A. N. and A. S. acknowledge Science and Engineering Research Board (SERB), India Projects No. ECR/2016/001967 and No. CRG/2019/005944, respectively, for financial support. M. C. and A. C. would like to thank Dr. R. Alert for sharing his stability calculations in Ref. [28].

---

[*] M. C. and A. C. contributed equally to this work.

[†] Present address: Physics Department, MIT, Cambridge, Massachusetts 02139, USA.

[‡] asain@phy.iitb.ac.in

[1] R. Rappaport, *Cytokinesis in Animal Cells* (Cambridge University Press, Cambridge, England, 1996).
[2] R. A. Green, E. Paluch, and K. Oegema, Annu. Rev. Cell Dev. Biol. **28**, 29 (2012).
[3] C. Guillot and T. Lecuit, Dev. Cell **24**, 227 (2013).
[4] H. Turlier, B. Audoly, J. Prost, and J.-F. Joanny, Biophys. J. **106**, 114 (2014).
[5] D. Bray and J. White, Science **239**, 883 (1988).
[6] J.-H. Zang and J. A. Spudich, Proc. Natl. Acad. Sci. U.S.A. **95**, 13652 (1998).
[7] A. Zumdieck, K. Kruse, H. Bringmann, A. A. Hyman, and F. Jülicher, PLoS One **2**, e696 (2007).
[8] A. Sain, M. M. Inamdar, and F. Jülicher, Phys. Rev. Lett. **114**, 048102 (2015).
[9] A. M. Silva, D. S. Osório, A. J. Pereira, H. Maiato, I. M. Pinto, B. Rubinstein, R. Gassmann, I. A. Telley, and A. X. Carvalho, J. Cell Biol. **215**, 789 (2016).
[10] G. Salbreux, J. Prost, and J.-F. Joanny, Phys. Rev. Lett. **103**, 058102 (2009).
[11] C. A. Mandato and W. M. Bement, J. Cell Biol. **154**, 785 (2001).
[12] A.-C. Reymann, F. Staniscia, A. Erzberger, G. Salbreux, and S. W. Grill, eLife **5**, e17807 (2016).
[13] F. Spira, S. Cuylen-Haering, S. Mehta, M. Samwer, A. Reversat, A. Verma, R. Oldenbourg, M. Sixt, and D. W. Gerlich, eLife **6**, e30867 (2017).
[14] Y. Li and E. Munro, Dev. Cell **56**, 2486 (2021).
[15] J. Leite, F.-Y. Chan, D. S. Osório, J. Saramago, A. F. Sobral, A. M. Silva, R. Gassmann, and A. X. Carvalho, Front. Cell Dev. Biol. **8**, 573393 (2020).
[16] T. Chen, A. Callan-Jones, E. Fedorov, A. Ravasio, A. Brugués, H. T. Ong, Y. Toyama, B. C. Low, X. Trepat, T. Shemesh *et al.*, Nat. Phys. **15**, 393 (2019).
[17] F. Juelicher, K. Kruse, J. Prost, and J.-F. Joanny, Phys. Rep. **449**, 3 (2007).
[18] See Supplemental Material at http://link.aps.org/supplemental/10.1103/PhysRevLett.128.068102 for more details. SI-part1: Derivation and solutions of the OP and the force balance equations. SI-part2: Stability calculation for the perturbed ring.
[19] P.-G. de Gennes and J. Prost, *The Physics of Liquid Crystals* (Oxford University Press, New York, 1993), Vol. 83.
[20] A. Carvalho, A. Desai, and K. Oegema, Cell **137**, 926 (2009).
[21] K. Kruse, J.-F. Joanny, F. Jülicher, J. Prost, and K. Sekimoto, Eur. Phys. J. E **16**, 5 (2005).
[22] M. C. Marchetti, J.-F. Joanny, S. Ramaswamy, T. B. Liverpool, J. Prost, M. Rao, and R. A. Simha, Rev. Mod. Phys. **85**, 1143 (2013).
[23] J. Prost, F. Jülicher, and J.-F. Joanny, Nat. Phys. **11**, 111 (2015).
[24] A. S. Maddox, L. Lewellyn, A. Desai, and K. Oegema, Dev. Cell **12**, 827 (2007).
[25] O. Thoumine, O. Cardoso, and J.-J. Meister, Eur. Biophys. J. **28**, 222 (1999).
[26] F. Wottawah, S. Schinkinger, B. Lincoln, R. Ananthakrishnan, M. Romeyke, J. Guck, and J. Käs, Phys. Rev. Lett. **94**, 098103 (2005).
[27] V. V. Menon, S. Soumya, A. Agarwal, S. R. Naganathan, M. M. Inamdar, and A. Sain, Biophys. J. **113**, 2787 (2017).
[28] C. Pérez-González, R. Alert, C. Blanch-Mercader, M. Gómez-González, T. Kolodziej, E. Bazellieres, J. Casademunt, and X. Trepat, Nat. Phys. **15**, 79 (2019).